

Anomalous electrochemical capacitance in Mott–insulator titanium sesquioxide

Sumana Kumar^{1†}, Sukanta Nandi^{1†}, Vikash Mishra², Alok Shukla², Abha Misra^{1‡}

¹Department of Instrumentation and Applied Physics, Indian Institute of Science, Bangalore, Karnataka 560012, India.

²Department of Physics, Indian Institute of Technology Bombay, Powai, Mumbai, Maharashtra 400076, India.

Abstract

Electrochemical capacitors with pure electric double layer capacitance are so far largely been limited to carbon materials only. Conventional metal oxides with Faradaic pseudocapacitance substantially suffer from the material instability at high temperatures and thus there is a demand of novel metal oxides exhibiting thermally improved high electric double layer capacitance with material stability. In this study, titanium sesquioxide, Ti_2O_3 , a Mott–insulator in its metallic state at 300 °C has shown an anomalous increase of ~560% in the solid–state electrochemical capacitance as compared to its pristine response at room temperature (RT). In aqueous electrolyte, the maximum capacitance was obtained up to 1053 $\mu F/cm^2$, which is 307% higher than with solid–state electrolyte. Moreover, the semiconducting state of Ti_2O_3 demonstrated ~3500% enhancement in its electrochemical capacitance upon infrared illumination at RT. The observed electrochemical responses in Ti_2O_3 are attributed to the transition of semiconducting to the metallic state by redistribution of the localized electrons. Our experimental results find a good agreement with the first–principles density–functional

[†] Both the authors have equal contribution.

[‡] Corresponding author, Email: abha.misra1@gmail.com

theory calculations that revealed an increase in the charge—density with the rise in temperature, which is mainly attributed to the surface Ti atoms. The study opens wide avenues to engineer the electrochemical double layer capacitance of Ti_2O_3 with high chemical stability.

Keywords: Titanium sesquioxide, Electrochemical supercapacitor, infrared, Mott-transition

Introduction

Fundamental limitations in batteries, like solid—state diffusion rate, phase transformations and the change in volume during charge/discharge have led to the preference of electrochemical capacitors, from the small—scale systems to large cells, for high rate energy transfer applications. Conway described the general requirement for the electrochemical capacitor materials as oxides with high electrical conductivity and exhibiting two or more oxidation states without a change in the phase.[1] First such widely studied materials are RuO_2 , IrO_2 and MnO_2 with pseudo—capacitive properties, where nonstoichiometry is mainly responsible for the electronic conductivity.[1] Moreover, electrochemical properties of these oxide films are highly dependent on their thickness, deposition temperature and mostly successful with aqueous electrolytes, thereby limiting their applications in the planar devices. The development of planar micro—scale electrochemical capacitor devices has established a direct connection with wearable smart devices covering a wide range of applications like health, environmental, industrial and transportation.[2] Thus, the quest for novel materials continues for a large electrochemical double layer capacitance and compatible with the planar micro—scale electrochemical capacitor devices.

Titanium oxides, the most abundant materials exhibit mixed valence states of Ti ions. Among these, titanium sesquioxide (Ti_2O_3) with Ti^{3+} ions and a narrow direct bandgap ($E_g \sim 0.11$ eV) has been studied recently for its photothermal characteristics[3] and long wavelength mid—infrared detection.[4] Ti_2O_3 also known as a Mott—insulator attains a metallic

conductivity at around 450 K without any change in its phase.[5] Vanadium oxides, another class of Mott–insulators with identical d^1 configuration are reported for their electrochemical capacitive behaviour in many works; however, poor stability severely affects their utility due to the lower transition temperature induced by the structural transition.[6,7] Therefore, higher transition temperature in Ti_2O_3 without structural transition is important for the devices operable under high-temperature conditions.

We report Ti_2O_3 based micro–electrochemical capacitor in a planar geometry as a novel electrode material. The granular Ti_2O_3 is directly spray-coated on a planar interdigitated electrode surface. Solid–state micro–electrochemical capacitance in the symmetric configuration is evaluated after annealing Ti_2O_3 in a wide temperature range from room temperature (RT) to 400 °C. An increase in areal electrochemical capacitance is observed in annealed Ti_2O_3 with a maximum enhancement of ~560% after annealing at 300 °C. Moreover, an optical interaction in the infrared (IR) range enhances the electrochemical capacitance to ~3500% in the pristine Ti_2O_3 . This anomalous increase in the electrochemical capacitance has not been reported so far in any metal oxide materials used for electrochemical capacitance thus, suggesting two distinct mechanisms contributing to electrochemical response in the Mott–insulator, Ti_2O_3 . A high capacitance retention of 80% in Ti_2O_3 device is achieved after 5000 cycles. Furthermore, the Ti_2O_3 device annealed at 300 °C in aqueous electrolyte exhibits areal capacitance of ~1050 $\mu F/cm^2$ at a scan rate of 1 mV/s. Our work demonstrated a promising strategy to rationally design and fabricate novel Ti_2O_3 material–based devices with largely enhanced capacitive behaviour.

Experimental details

The granular powder of Ti_2O_3 was commercially procured from Sigma–Aldrich with particle size of 100 mesh as inferred from the scanning electron microscope (SEM) micrographs (for an example Figure S1). Dispersion of 200 mg Ti_2O_3 is prepared in 30 ml of ethanol by

ultrasonication for 6 hours. The electrochemical performance of Ti₂O₃ was analysed using planar interdigitated gold electrodes deposited on a glass substrate with 20/200 nm thick chromium/gold (Cr/Au) layers for both the anode and the cathode. Each electrode consists of four fingers and the dimension of each finger is 1x13 mm² with an active electrode area of 2.4 cm². The mass loading on microelectrodes was 2.2 mg/cm². The dispersion of Ti₂O₃ was spray coated on both the electrodes and prior to the electrochemical measurements, the spray coated electrodes were annealed at 200 °C, 300 °C and 400 °C for 6 hours.

Results and Discussion

Detailed characterizations were conducted to elucidate the effect of annealing on the granular Ti₂O₃. The X-ray diffraction (XRD) of Ti₂O₃ confirmed the corundum crystal structure due to the presence of corresponding crystalline planes (101), (012), (104), (110), (006), (113), (202), (024), (116), (122), (214), (300), (1010), (220), (306) and (312) at $2\theta = 20.71^\circ, 23.82^\circ, 33.05^\circ, 34.82^\circ, 39.67^\circ, 40.23^\circ, 43.02^\circ, 48.70^\circ, 53.78^\circ, 56.21^\circ, 61.33^\circ, 62.44^\circ, 72.43^\circ, 73.54^\circ, 76.58^\circ$ and 78.61° , respectively at all the thermal conditions (figure 1(a) and figure S2).[3,8,9] The remaining peaks indicated by * are identified as other thermally stable TiO_x phases and do not reveal any variations due to the annealing at any temperature.[10] The lattice parameters *a*, *b* and *c* of a trigonal cell in the $R\bar{3}c$ corundum crystal of Ti₂O₃ deduced from XRD analysis at RT are $a=b=5.146 \text{ \AA}$ and $c=13.636 \text{ \AA}$. The parameters *c*, *a* and the ratio *c/a* at different annealing temperatures are shown in figure 1(b). The change in *c* and *a* parameters of Ti₂O₃ with annealing temperature is shown to follow the linear and nonlinear variations, respectively in the upper figure in 1(b). The value of *a* changes marginally from 5.146 (RT) to 5.145 Å (400 °C), while that of *c* changes considerably from 13.636 (RT) to 13.643 Å (400 °C). A large variation in *c* leads to a higher change in the ratio *c/a*, being 2.652 at 400 °C (the lower figure in 1(b)) compared to other annealing conditions. Moreover, in agreement with the previous studies,[5] no additional peaks are observed in Ti₂O₃ after annealing at 200 °C and 300 °C

(figure 1(c)), thus confirming no impurity phases in Ti_2O_3 . However, at 400 °C, a peak corresponding to (110) plane of rutile titanium dioxide (TiO_2) appeared at $2\theta=27.48^\circ$, as shown in figure 1(d). Furthermore, a close inspection of (300) plane is depicted in figure 1(e–h) from RT to 400 °C. There is no peak corresponding to (002) plane of rutile TiO_2 at both RT and 200 °C as depicted in Figures 1(e) and (f). However, at 300 °C, a secondary peak corresponding to (002) plane of rutile TiO_2 appears as shown by an arrow in figure 1(g), which became prominent at 400 °C. Figure 1(h) prominently depicts a peak at 62.38° for (002) plane of rutile TiO_2 at 400 °C along with (300) plane of Ti_2O_3 at 62.48° . [11]

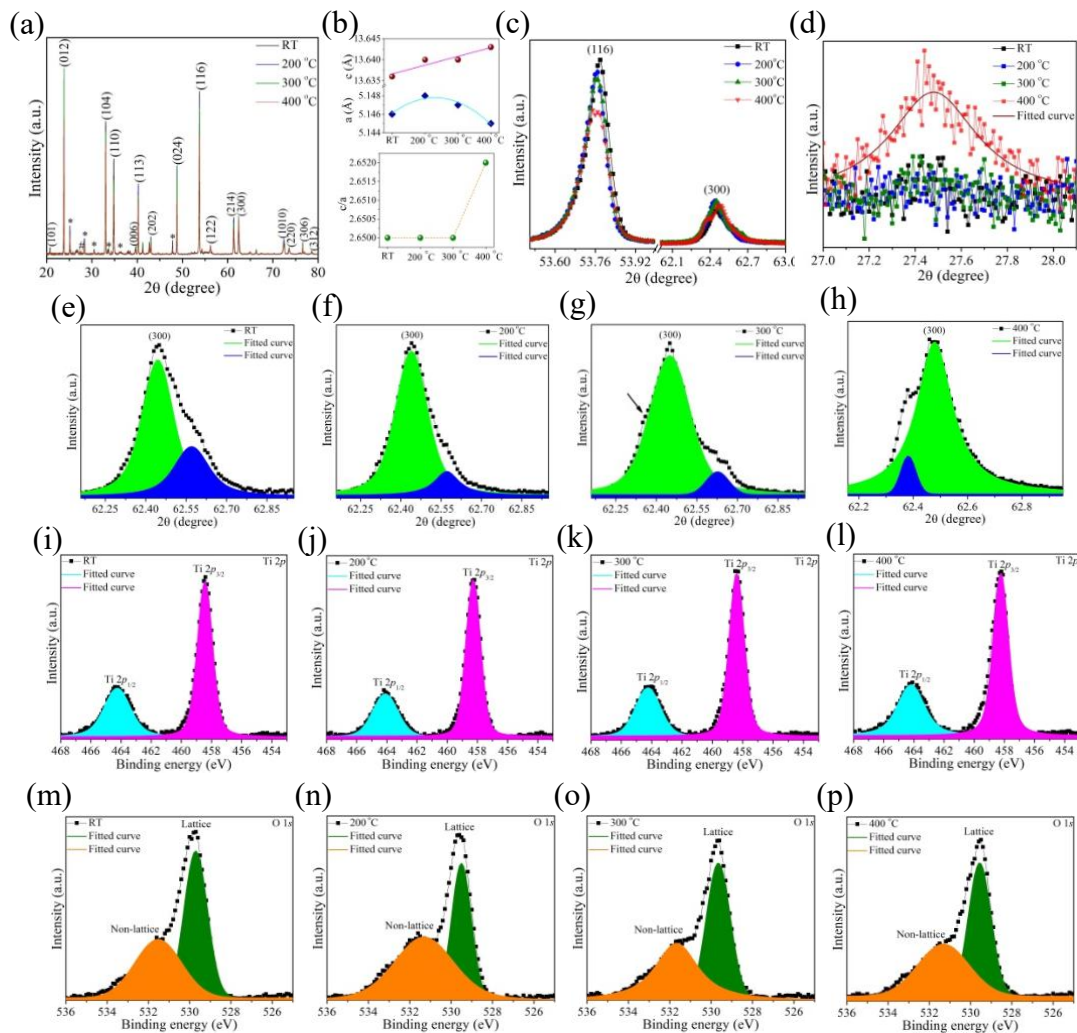


Figure 1. (a) XRD spectra of pristine Ti_2O_3 and after annealing at 200 °C, 300 °C and 400 °C. (b) Lattice parameters c and a evaluated from the XRD analysis are plotted with the annealing temperature (top and bottom, respectively). (c) (116) and (300) planes of Ti_2O_3 at heating

conditions. (d) Zoomed-in XRD spectra showing emergence of (110) plane of rutile TiO₂ in annealed Ti₂O₃ at 400 °C and compared with other heating conditions. (e)–(h) A systematic modification is depicted alongside (300) plane of Ti₂O₃ at both RT and annealed temperatures. XPS spectra of pristine Ti₂O₃ at RT and annealed at 200 °C, 300 °C and 400 °C to show the electronic states respectively of Ti in (i–l) and the corresponding spectra for O in (m–p).

Electronic states of the constituent elements (Ti and O) of Ti₂O₃ at different heating conditions are probed with X-ray photoelectron spectroscopy (XPS) as depicted in figure 1(i–p). It is observed in figure 1(i) that Ti is in +3 state with the spin-orbit splitting resulting in the electronic states of Ti 2p_{3/2} (458.4 eV) and Ti 2p_{1/2} (464.2 eV).[4,8] The peak positions are monitored in different annealed samples without any noticeable differences *e.g.* the peak for Ti 2p_{3/2} at RT shifts from 458.4 eV (figure 1(i)) to 458.2 eV at 400 °C (figure 1(l)). The oxygen on the other hand is in O 1s state, with the peak position at 529.7 eV (figure 1(m)) owes its origin from Ti–O bonds in the lattice of Ti₂O₃. [4,8] In addition, a secondary peak (non-lattice) at 531.5 eV (figure 1(m)) is also observed that could be originated from the distorted Ti₂O₃ structure.[5,8] Similar to the Ti peak shifts, there are no observable peak shift noted with O at the different annealing temperatures *e.g.* the lattice peak of O at 529.7 eV at RT (figure 1(m)) only changes to 529.6 eV at 400 °C (figure 1(p)). The peak positions at all the annealing temperatures are provided in figure S3(a) for the Ti and figure S3(b) for the O spectra.

The SEM image in figure 2(a) depicts the surface of the pristine Ti₂O₃ and a change in the surface morphology after annealing at 400 °C is clearly revealed in figure 2(b), with nanostructures as suggested by Li *et al.* in their report.[5] The change in surface morphology can be attributed to the phase transformation of Ti₂O₃ to rutile TiO₂ with a Ti₂O₃/TiO₂ core-shell structure.[5,12] However, the samples annealed at 200 °C and 300 °C do not show any observable morphological differences on the surface (figure S4).

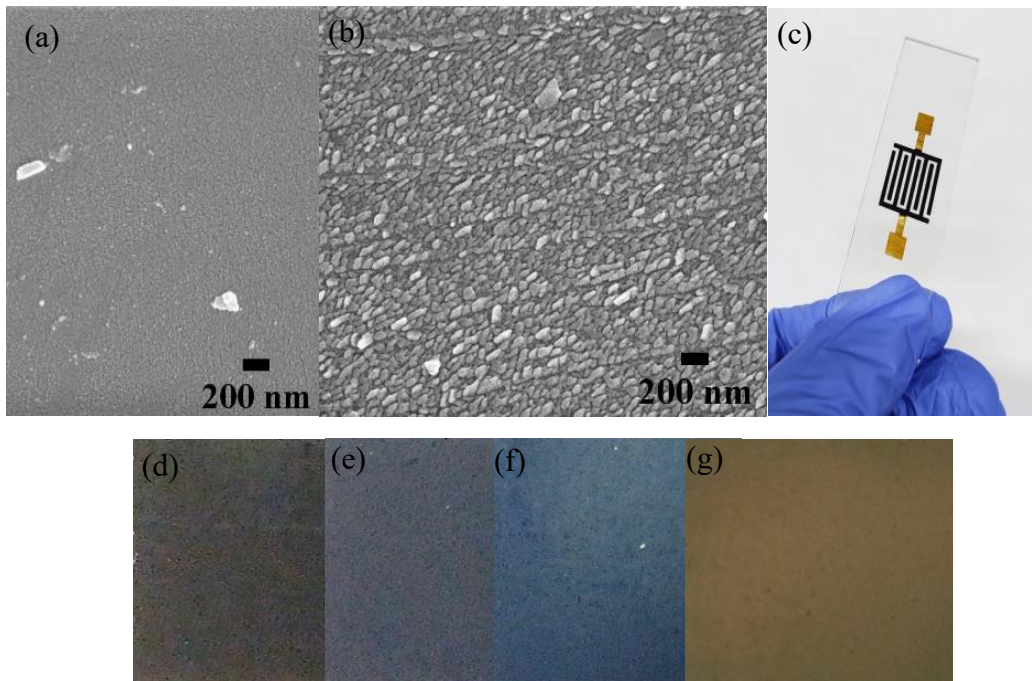


Figure 2. SEM images of (a) pristine Ti_2O_3 and after annealing at 400 °C (b). (c) Digital image of the spray-coated interdigitated planar device. Optical images (at same magnification) are showing a change in the colour of pristine Ti_2O_3 (d) at RT along with the annealing temperature at (e) 200 °C, (f) 300 °C, and (g) 400 °C.

The optical images in figure 2(d–g) show a change in colour of the surface of pristine Ti_2O_3 (figure 2(d)) after annealing at 200 °C (figure 2(e)), 300 °C (figure 2(f)) and 400 °C (figure 2(g)). A drastic change in colour is observed at an annealing temperature of 400 °C compared to other annealing conditions for Ti_2O_3 . These results agree with both the XRD measurements and a report by Li *et al.*, where the formation of Ti^{4+} layer on the surface of Ti_2O_3 is reported even at RT, which becomes prominent after annealing.[5] Energy dispersive X-ray analysis (figure S5) revealed a decrease in the intensities of both Ti and O at 400 °C. An apparent surface modification in Ti_2O_3 is revealed in both the optical and SEM images, which is supported by

the XRD and XPS measurements, thus showing only surface modifications without any dominant new phase due to the annealing of Ti_2O_3 .

Further, density functional theoretical (DFT) calculations were performed to understand the impact of annealing on electronic transition in Ti_2O_3 . Details of simulation parameters are provided in the supporting information. All electronic properties of Ti_2O_3 were calculated using lattice parameters derived from the temperature–dependent XRD data. Figure 3(a) shows an indirect band diagram of Ti_2O_3 at RT with a bandgap of 0.11 eV (at Γ –Z points), which is shown to decrease with the increase in the temperature.

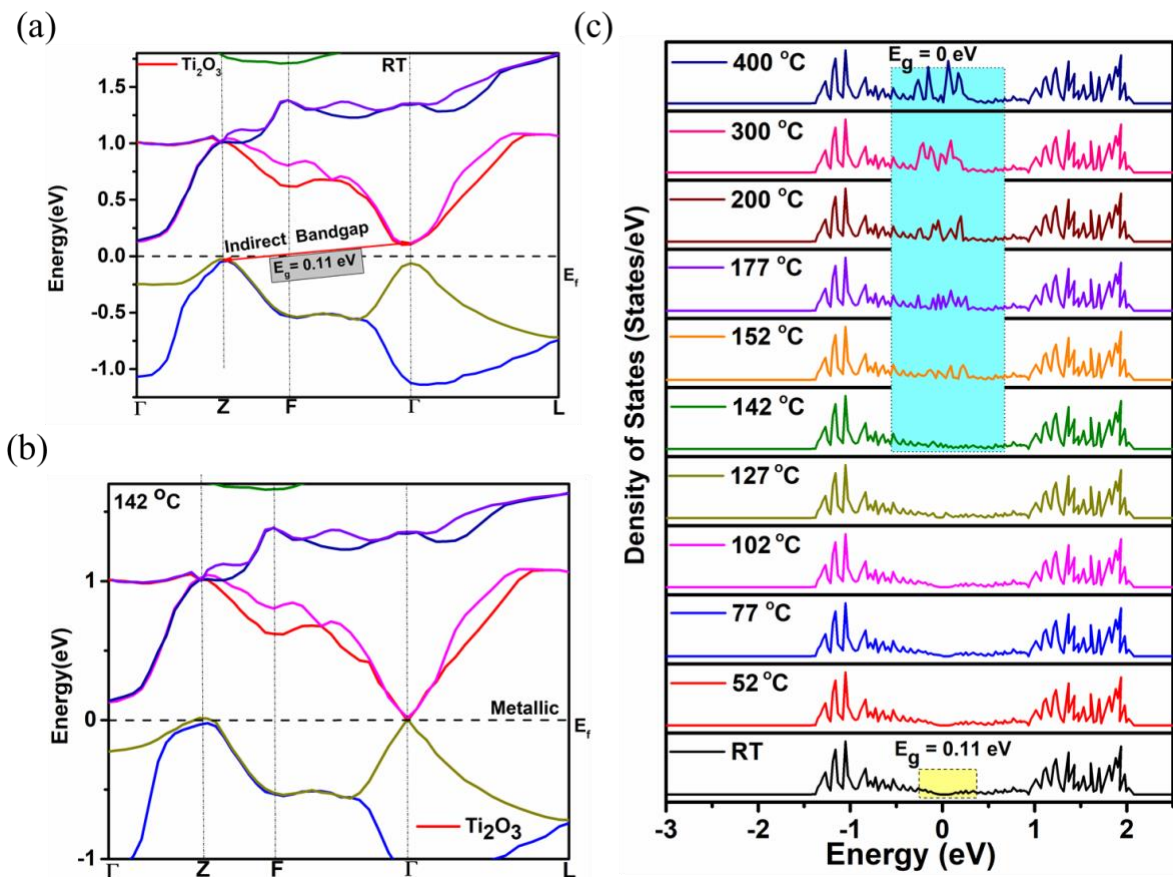


Figure 3. Band structure of Ti_2O_3 at (a) RT (b) at 142 °C. (c) Total DOS of Ti_2O_3 at different temperatures and shows the presence of bandgap in the range from RT to 142 °C.

A band merging ($E_g = 0$) is observed at around 142 °C and thus a transition to a metallic state of Ti_2O_3 can be seen at Γ point (figure 3(b)).[13] The HSE06[14] calculations were performed

for the total density of states (TDOS) of Ti_2O_3 to evaluate a modification in E_g with the temperature variation in the range from RT to 400 °C (figure 3(c)).

It is observed that the E_g decreases gradually with an increase in the temperature and a complete metallic transition is observed at a temperature of ~ 142 °C, which is attributed to the emergence of new states between the conduction band maxima (CBM) and valence band minima (VBM). Figure S6(a) clearly shows a variation in bandgap with temperature and a metallic transition around 142 °C in Ti_2O_3 . Figure S6(b) shows the partial density of states (PDOS) at RT, where the electrons of Ti–Ti bonding are highly populated near VBM and CBM. It is important to note that the metallic behaviour in Ti_2O_3 is mainly due to the hopping of the $3d$ electrons in the Ti–Ti bond. The electronic phase transition therefore arises from a delicate balance between the width and energy position of Ti– $3d$ sub-bands along with the variation in Ti–Ti bond length. At RT, the states near Fermi level (E_f) are dominated by Ti– $3d$ orbitals (figure S6(b)), suggesting a strong hybridization [15,16] between of Ti–Ti bonding due to $3d$ orbitals. [13] Furthermore, a closer inspection of the density of states near E_f (at higher temperature (see figure S6(c)) revealed a dominant participation of Ti– $3d$ orbitals in the formation of Ti–Ti bonding than Ti–O bond arising due to the interaction with O– $2p$ orbitals. This further confirms the finding in XPS results. The Bader charge analysis has also been carried out in the VASP CHGCAR using charge densities grid and shown in Table S1 & S2. The charge analysis further reveals an increase in the charge–density with the rise in temperature, which is mainly attributed to the surface Ti atoms. On the contrary, the charge–density remains unchanged for the bulk Ti atoms (i.e. inner atoms) and all the O atoms.

The increase in charge density on the surface of Ti_2O_3 is further exploited to study the electrochemical capacitance due to the formation of electric double layer on the surface of the electrodes. Figure 2(c) depicts the planar interdigitated electrodes after spray coating of pristine Ti_2O_3 in a symmetric configuration. The micro–electrochemical capacitor is fabricated by

drop-casting PVA/H₃PO₄ (poly(vinyl alcohol)/phosphoric acid) solid gel electrolyte. The gel was prepared by the method described elsewhere.[17] Both the electrodes were directly probed with the CHI600E electrochemical station. The electrochemical performance of Ti₂O₃ devices annealed at different temperatures was measured using cyclic voltammetry (CV) at various scan rates ranging from 5 mV/s to 1000 mV/s (figure 4(a)–(d)). A rectangular shape of CV without redox peaks is observed in both the pristine as well as annealed Ti₂O₃ based electrochemical capacitors. Therefore, it clearly indicates the presence of a large capacitive response at the interface of electrode material surface and electrolyte.

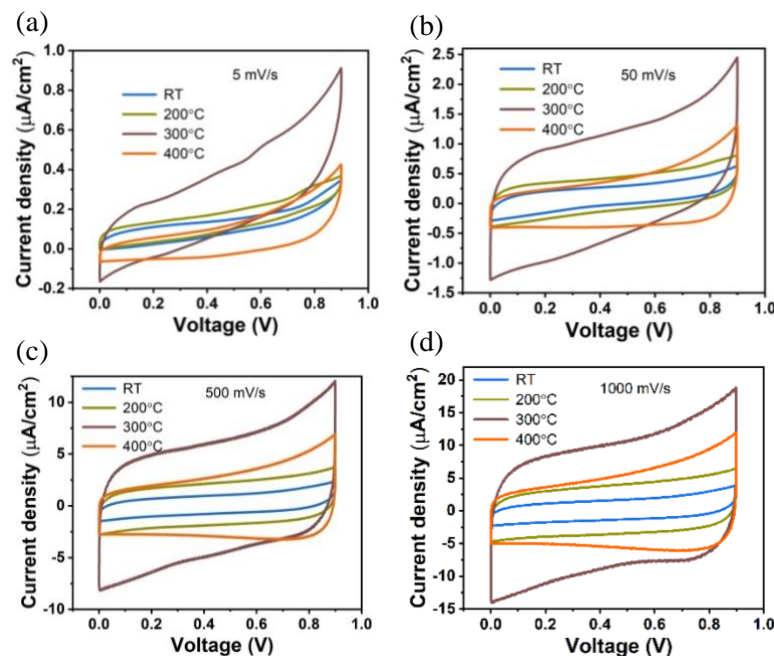


Figure 4. CV curves of the planar interdigitated electrochemical capacitor evaluated with pristine and annealed Ti₂O₃ devices at the scan rate of (a) 5 mV/s, (b) 50 mV/s, (c) 500 mV/s, and 1000 mV/s.

The rectangular shape of CV at a high scan rate further indicates a low internal resistance and high rate capability of the capacitor. Therefore, the electrochemical behaviour of Ti₂O₃ is unconventionally different from materials like RuO₂ and MnO₂, where distorted CV curves

were obtained due to the presence of higher pseudocapacitance. Moreover, a high-temperature electrochemical stability of Ti_2O_3 is attributed to its high structural stability till 300°C .

Total charge storage in the Ti_2O_3 devices can be distinctly deconvoluted into two components: electrical double layer capacitance (EDLC) and diffusion-controlled processes (pseudocapacitance) using Dunn's method.[18][19] In the CV curve, the current response (i) at a fixed potential (V) can be expressed as the sum of the two separate mechanisms, namely surface capacitive effects (k_1v) and diffusion-controlled process ($k_2v^{1/2}$) according to the following relation:

$$i(V) = k_1v + k_2v^{1/2} \quad (1)$$

$$\text{or} \quad \frac{i(V)}{v^{1/2}} = k_1v^{1/2} + k_2 \quad (2)$$

where v is the scan rate.[18] By determining k_1 and k_2 in equation 2, a separate contribution is evaluated from the current arising from diffusion-controlled process and surface capacitive process at specific potentials. Figure 5(a)-(d) exhibit the capacitive and diffusion-controlled contribution in pristine and annealed Ti_2O_3 devices at a scan rate of 100 mV/s .

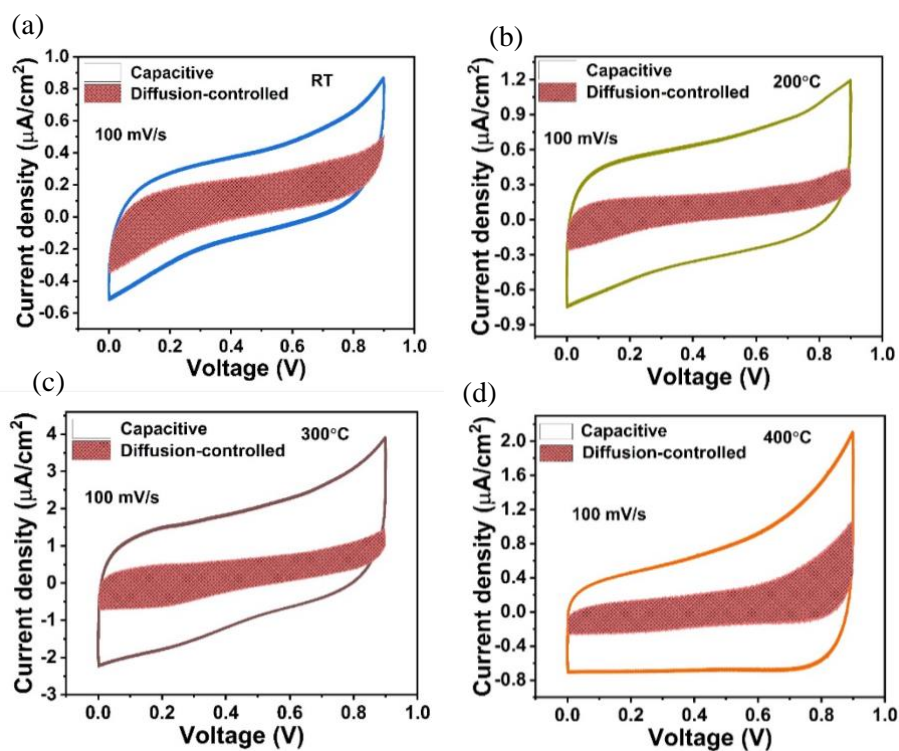


Figure 5: CV curve shows the capacitive and diffusion-controlled charge storage contributions at 100 mV/s scan rate in pristine Ti₂O₃ devices, (a) at RT, and annealed at (b) 200 °C, (c) 300 °C (d) 400 °C.

Figure 6(a)-(d) exhibit a typical separation of capacitive and diffusive contribution in pristine and annealed Ti₂O₃ devices at low scan rates of 5, 20, 50 and 100 mV/s. As shown in figure 6(a), the surface capacitive controlled process contributes 19%, 30%, 41% and 50% of the total charge at 5, 20, 50 and 100 mV/s, respectively for pristine Ti₂O₃ devices at RT, suggesting the dominant diffusion-controlled charge storage mechanism at lower scan rate. Although, there are no evident peaks in the CV responses, proton diffusion could contribute to the observed charge enhancement. Moreover, the surface capacitive contribution increases with increase of scan rate.

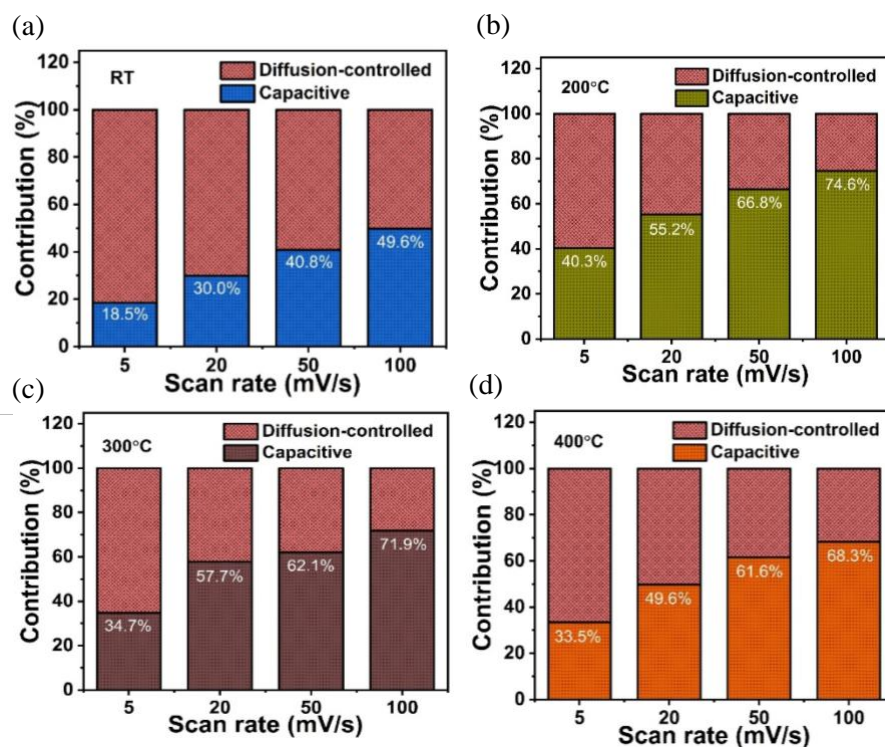


Figure 6: Capacitive and diffusion-controlled charge storage contribution at different scan rates of pristine Ti_2O_3 devices, (a) at RT, and annealed Ti_2O_3 devices at (b) 200 °C, (c) 300 °C (d) 400 °C.

It is noteworthy that upon annealing, the surface capacitive effect increases at all temperatures, resulting in significantly fast charge storage along with long term cyclic stability. Also, the increase in surface-capacitive contribution with increasing scan rate is observed after annealing of Ti_2O_3 devices and at higher scan rate of 100 mV/s, the charge storage mechanism is dominantly capacitive.

The areal capacitance or energy density are more suitable performance metrics for electrochemical response analysis compared to traditional gravimetric capacitance because the mass of active material is negligibly small compared with the mass of the whole device.[20]

The areal capacitance of micro—electrochemical capacitors was calculated from the CV curves obtained at various scan rates by considering the area of both the interdigitated electrodes and the gap between adjacent fingers.

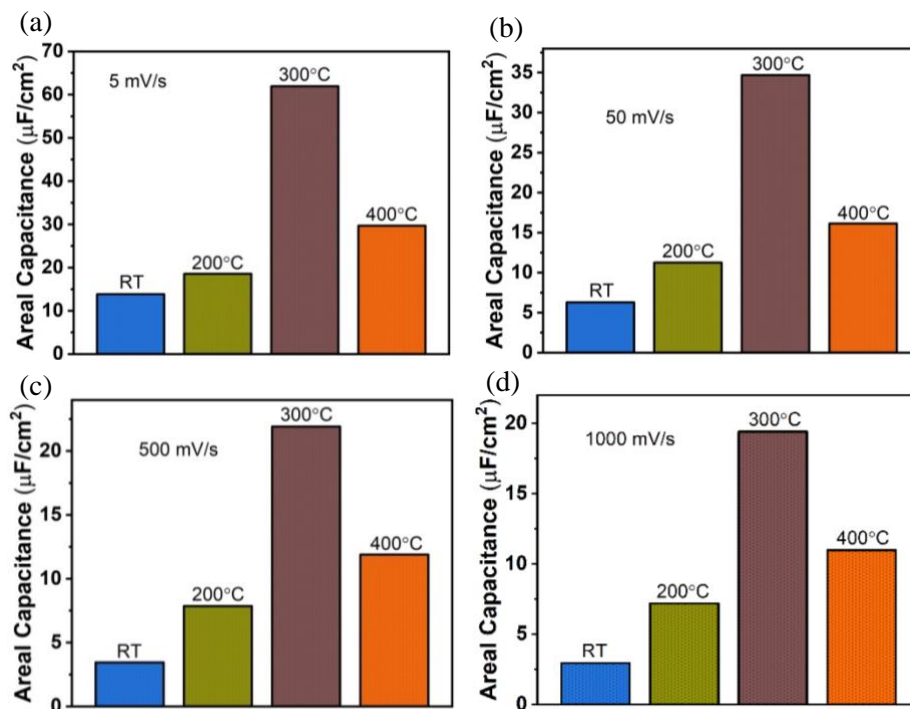


Figure 7. Areal electrochemical capacitance of pristine Ti₂O₃ and annealed at 200 °C, 300 °C and 400 °C at the scan rate of (a) 5 mV/s, (b) 50 mV/s, (c) 500 mV/s and 1000 mV/s.

Figure 7 summarises the calculated areal electrochemical capacitance at the four scan rates (5–1000 mV/s). As evident from figure 7(a–d) that at all the scan rates, the electrochemical capacitance is dominated by annealed Ti₂O₃ at 300 °C. The pristine Ti₂O₃ device showed an areal capacitance of about 13.84 μF/cm² at a scan rate of 5 mV/s, which reduced to 6.28 μF/cm² at a scan rate of 50 mV/s. Moreover, capacitance further dropped to 3.45 and 2.95 μF/cm² at the higher scan rates of 500 mV/s and 1000 mV/s, respectively. The capacitance at 500 mV/s and 1000 mV/s is about 24.9% and 21.3% of its initial capacitance at the scan rate of 5 mV/s. An enhancement of 34.24% in electrochemical capacitance is observed after annealing of granular Ti₂O₃ at 200 °C at a scan rate of 5 mV/s. The Ti₂O₃ device annealed at 300 °C showed an areal electrochemical capacitance of about 61.96 μF/cm² at a scan rate of 5 mV/s, which reduced to 29.96 μF/cm² at a scan rate of 100 mV/s. Moreover, capacitance dropped to 21.92 and 19.41 μF/cm² at the higher scan rates of 500 mV/s and 1000 mV/s, respectively. However, in Ti₂O₃ device after annealed at 300 °C, an anomalous increase of 559% is observed at a scan rate of 1000 mV/s and 347% after decreasing the scan rate to 5 mV/s compared with the pristine Ti₂O₃. An extremely large enhancement of 1153% in electrochemical capacitance was observed after ball–milling of the pristine granular Ti₂O₃ and annealed at 300 °C compared to pristine Ti₂O₃ device (without ball–milling) (figure S7(a)) and 180% enhancement when compared to pristine Ti₂O₃ device annealed at 300 °C (figure S7(b)). The enhancement is clearly attributed to the reduced particle size distribution providing higher accessible sites for the electrolyte (figure S7(c)). The high specific surface area of ball–milled Ti₂O₃ (12.5 m²/g) than pristine Ti₂O₃ (0.283 m²/g) is confirmed by Brunauer–Emmett–Teller (BET) surface area measurement using nitrogen gas adsorption and desorption. The ball–milled Ti₂O₃ device

exhibited a high capacitance of $173.5 \mu\text{F}/\text{cm}^2$ at $5 \text{ mV}/\text{s}$, which reduced to $73.62 \mu\text{F}/\text{cm}^2$ at $50 \text{ mV}/\text{s}$ (figure S7(d)).

The electrochemical capacitor response of thermally stable phases of the Ti_2O_3 (Mott-insulator) after ex-situ annealing is evaluated and compared with the earlier reports; where annealing of graphene coated with V_2O_5 , categorized as Mott–insulator, demonstrated a continuous decay in electrochemical capacitance to $\sim 63\%$ with the increase in the temperature till $500 \text{ }^\circ\text{C}$. [21] Moreover, hydrous RuO_2 powder exhibits a sharp decay in the electrochemical capacitance when annealing temperature exceeded $150 \text{ }^\circ\text{C}$, in a temperature range of 25 to $400 \text{ }^\circ\text{C}$ and the reported decrease in the specific capacitance was 2644% . [22]

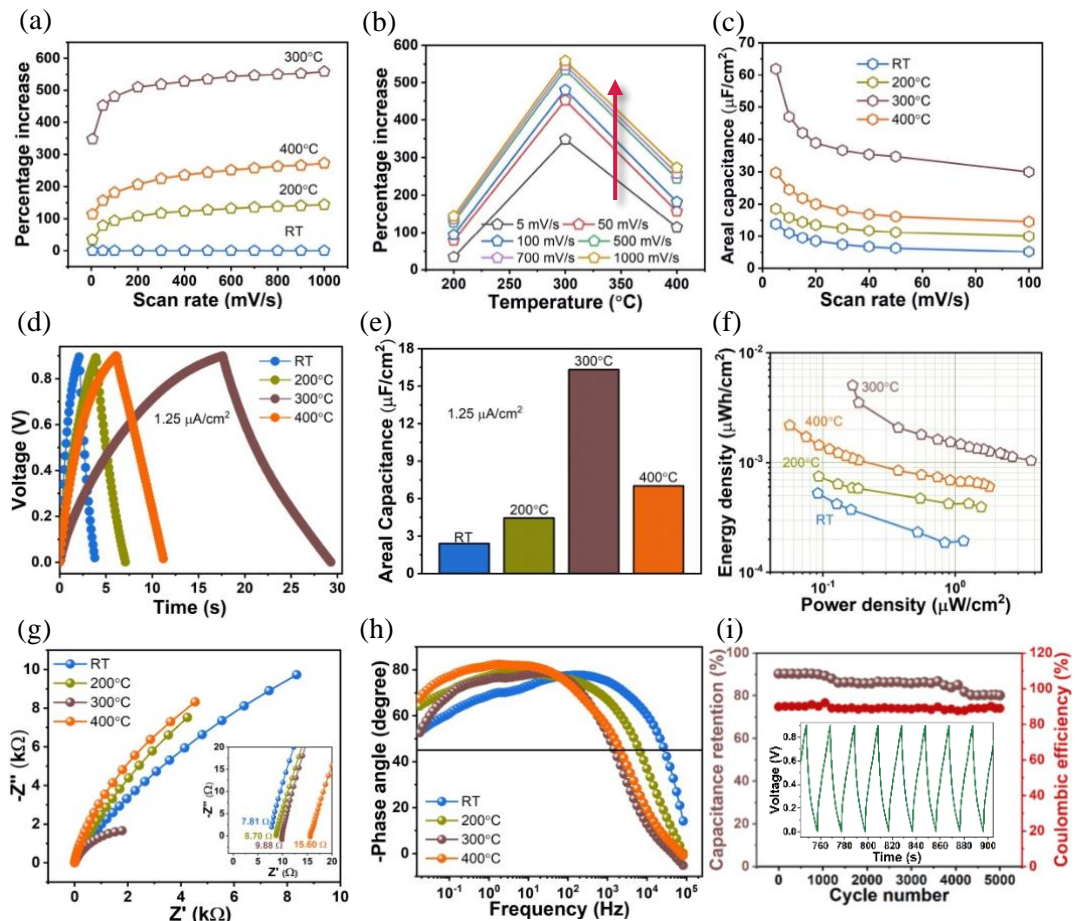


Figure 8. Electrochemical parameters of the Ti_2O_3 devices at different heating conditions: (a) Percentage increase in the electrochemical capacitance after annealing is measured with respect

to the pristine Ti_2O_3 at different scan rates. (b) Percentage increase in the electrochemical capacitance is measured with respect to the pristine response of the Ti_2O_3 at different annealing conditions. (c) Areal capacitance is shown at various scan rates. (d) Charge–discharge curves and (e) areal electrochemical capacitance at a current density of $1.25 \mu\text{A}/\text{cm}^2$. (f) Ragone plot of Ti_2O_3 devices under various annealing conditions. (g) AC impedance spectroscopy of Ti_2O_3 devices; inset depicts a zoom–in view at high–frequency region. (h) Bode plot of the Ti_2O_3 devices. (i) Capacitance retention and Coulombic efficiency of Ti_2O_3 device annealed at 300°C plotted for 5000 cycles; inset depicts a few charge-discharge cycles.

Figure 8(a) depicts the percentage enhancement in electrochemical capacitance from RT to annealed Ti_2O_3 devices at 200°C , 300°C and 400°C at the scan rates ranging from 5 to 1000 mV/s. Although the device annealed at 400°C has higher electrochemical capacitance than the device annealed at 200°C , but it remains lower compared to the device annealed at 300°C at all the scan rates. Moreover, the electrochemical capacitance of Ti_2O_3 after annealing is enhanced compared to the pristine device at all the scan rates. A faster increase in the electrochemical capacitance is observed at the lower scan rates, while all the devices showed a slow increase at higher scan rates. Figure 8(b) clearly depicts a sharp increase in the percentage enhancement of electrochemical capacitance of Ti_2O_3 annealed at 300°C at all the scan rates. Further, the areal electrochemical capacitance is shown to decrease with the scan rate measured in the range of 5–100 mV/s (figure 8(c)) in all the Ti_2O_3 devices.

The performance of Ti_2O_3 devices was further evaluated by measuring the galvanostatic charge–discharge (CD) curve at various applied current densities. The CD curves show a triangular shape, which is a typical EDLC behaviour at a current density of $1.25 \mu\text{A}/\text{cm}^2$ (figure 8(d)). A sudden drop in the voltage (IR drop) at the beginning of the discharge curves is a measure of the overall resistance of the device.[23] A small IR drop in all the devices after

annealing indicates a very low internal resistance and the values are given by 0.0271, 0.0103 and 0.0094 V for the devices annealed at 200 °C, 300 °C, and 400 °C, respectively (figure S8(a)). The areal specific capacitances were also calculated from the CD curves and plotted as shown in figure S8(b). A higher electrochemical capacitance at all the current densities was achieved for the Ti₂O₃ device annealed at 300 °C, which is in good agreement with CV results. The pristine Ti₂O₃ device showed a maximum areal capacitance of 9.52 μF/cm² at a current density of 0.167 μA/cm². The maximum areal capacitance of annealed Ti₂O₃ device (300 °C) is measured 45.2 μF/cm² at a current density of 0.37 μA/cm², which reduced to 10.21 μF/cm² at much increased current density of 8.75 μA/cm². Electrochemical capacitance from the CD measurement of Ti₂O₃ devices is compared in figure 8(e), which shows an enhancement of 580% for the Ti₂O₃ device annealed at 300 °C from pristine Ti₂O₃ device at a current density of 1.25 μA/cm². Therefore, CD measurements further confirm the annealing effect on the electrochemical capacitance of granular Ti₂O₃, where the electrochemical capacitance of the sample annealed at 400 °C sharply dropped by 132% from the sample annealed at 300 °C. Further enhancement in electrochemical capacitance was observed in ball-milled Ti₂O₃, where the device annealed at 300 °C exhibited an areal capacitance of 183.37 μF/cm² at 1.04 μA/cm² current density, which reduced to 13.57 μF/cm² at a current density of 20.84 μA/cm² (figure S8(c)). A further enhancement of 584% is noted in annealed ball-milled Ti₂O₃ device compared to annealed Ti₂O₃ device at a current density of 1.25 μA/cm², when both the devices are annealed at 300°C (figure S8(d)).

Areal energy density and power density of all the four devices, including pristine Ti₂O₃, were calculated from the CD curve at various current densities and shown in the Ragone plot (figure 8(f)). The measured drop in energy density with increasing power density is small, as evident in the plot. The pristine Ti₂O₃ device demonstrated an areal energy density of 1.034 nWh/cm² at a power density of 73.66 nW/cm² and 0.193 nWh/cm² at 1159.3 nW/cm². The

Ragone plot of Ti₂O₃ device annealed at 300 °C shows substantially higher energy density compared to the other three devices. For instance, the Ti₂O₃ device (annealed at 300 °C) achieved a maximum energy density of 5.04 nWh/cm² at a power density of 168 nW/cm² and a maximum power density of 3749.3 nW/cm² is noted at the energy density of 1.041 nWh/cm². For quantitative analysis, the areal energy density is plotted in a bar diagram at a current density of 1.25 μA/cm² for all the four Ti₂O₃ devices (figure S9(a)). The Ti₂O₃ device annealed at 300 °C exhibited 675.75% enhancement in areal energy density compared to pristine one (figure S9(b)). Furthermore, an enhancement of 549% in the areal energy density was observed in ball-milled Ti₂O₃ device, compared to without ball-milled and annealed at 300 °C (figure S9(c)). The ball-milled Ti₂O₃ device annealed at 300 °C attains a high energy density of 19.23 nWh/cm² at a power density of 452.6 nW/cm² and a maximum power density of 8010.4 nW/cm² at the energy density of 1.11 nWh/cm² (figure S9(d)).

Electrochemical impedance spectroscopy was performed in terms of Nyquist and Bode plots to further provide an insight in the ohmic and diffusion resistances of ions in the electrodes for all the four devices (figures 8(g) and (h)). The equivalent series resistance values of pristine and annealed Ti₂O₃ devices, as shown in the inset of figure 8(g) are 7.81, 8.70, 9.88, and 15.60 Ω thus, showing a good electrochemical conductivity of all the devices. A semi-circular arc is observed only at 300 °C, which explains the space charge polarization. The dependence of phase angle with frequency (Bode plot) in the Ti₂O₃ devices was further presented in figure 8(h) for informative analysis of impedance spectroscopy. For frequencies up to 100 Hz, all the phase angles of Ti₂O₃ devices are close to 90°; after that, the phase angle decreases with an increased frequency. In addition, the characteristics frequency (f_0) at a phase angle of -45° indicates that the resistive and capacitive impedances are equal and later, resistive behaviour dominates.[23] As shown in figure 8(h), the characteristics frequency of pristine Ti₂O₃ is 27711.35 Hz, and 6463.05, 1505.42 and 2136.5 Hz for Ti₂O₃ devices annealed at 200 °C, 300

°C, and 400 °C, respectively. Therefore, the corresponding relaxation time constant $\tau_0 (= 1/f_0)$, defined as the minimum time required to discharge all the energy from the device with an efficiency greater than 50%, [24,25] is 0.036 ms for pristine Ti_2O_3 , in contrast to 0.154, 0.664, and 0.468 ms for Ti_2O_3 devices annealed at 200 °C, 300 °C and 400 °C, respectively. The obtained time constant for Ti_2O_3 devices is promising compared to the previously best-reported value for the EDLC based micro electrochemical capacitors, such as activated carbon (700 ms), [24] onion like carbon (26 ms), [24] laser reduction graphene (19 ms) [26], and graphene/CNT composite (3.4 ms). [23] Furthermore, the cyclic life of Ti_2O_3 device annealed at 300 °C was evaluated by long term charging and discharging cycle over 5000 cycles at a current density of $0.167 \mu\text{A}/\text{cm}^2$ (figure 8(i)). A high Coulombic efficiency of 89% is measured, while, capacitance retention was maintained 80% after 5000 cycles.

Semiconductor Ti_2O_3 with a bandgap of 0.11 eV further allows radiation interaction in the IR range. The electrochemical measurements were performed in the presence of IR radiation using a bulb (Philips Infrared–R95E). The light interaction further improved the electrochemical capacitance of both pristine and annealed Ti_2O_3 devices. Figure 9(a) shows the CV measurement of pristine Ti_2O_3 device at three conditions of before and after IR illumination for 30 minutes and the measurement conducted after 24 h of illumination. Figure 9(b) summarises the enhanced electrochemical capacitance of all the Ti_2O_3 devices compared to without IR illumination.

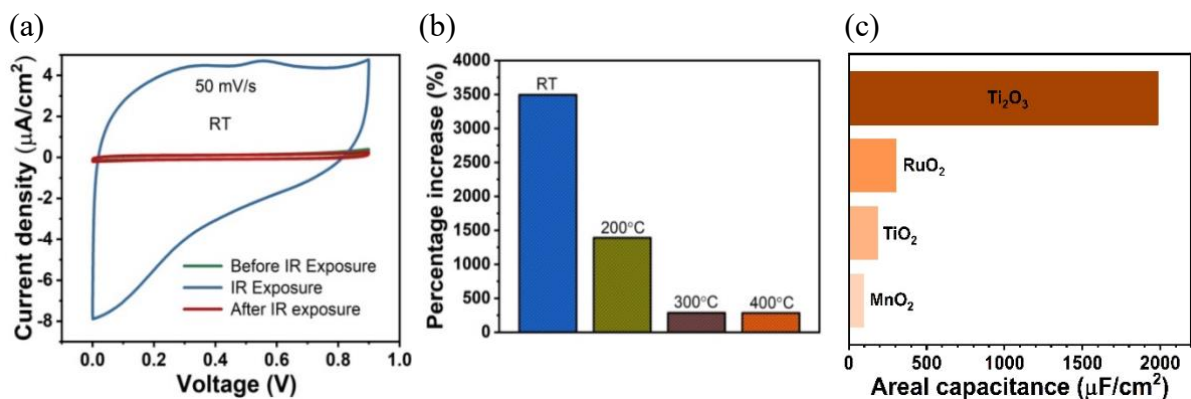


Figure 9. (a) CV curves of pristine Ti_2O_3 device before, in presence of IR and after IR interaction. (b) The percentage enhancement in electrochemical capacitance upon IR interaction is measured at various thermal conditions compared to without illumination condition. (c) Areal capacitance of ball-milled Ti_2O_3 electrode (annealed at $300\text{ }^\circ\text{C}$) using three-electrode configuration in $1\text{M H}_3\text{PO}_4$ compared with previously reported literature.

Under IR illumination, an enormously large enhancement of 3494% is observed in the pristine Ti_2O_3 device at a scan rate of 50 mV/s . The effect of metallic transition with heating is clearly confirmed with the decay in the electrochemical response of the annealed Ti_2O_3 devices upon IR illumination. A much larger enhancement in electrochemical capacitance upon IR interaction does not have any impact on electrochemical characteristics of the device as shown in figure S10, where all the samples exhibited reversible behaviour after turning off the IR illumination.

Furthermore, the electrochemical performance of ball-milled Ti_2O_3 device annealed at $300\text{ }^\circ\text{C}$ is also characterized in aqueous H_3PO_4 electrolyte. The measured areal capacitances from the CV curves are 1052.7 and $706.5\text{ }\mu\text{F/cm}^2$ at a scan rate of 1 and 5 mV/s , respectively. Also, the electrochemical performance of ball-milled Ti_2O_3 material (annealed at $300\text{ }^\circ\text{C}$) analysed using a three-electrode configuration in $1\text{M H}_3\text{PO}_4$ electrolyte (details are in supporting information). The measured capacitance from the CV curve is 2409 mF/g ($1985\text{ }\mu\text{F/cm}^2$) at a scan rate of 1 mV/s as shown in figure S11. The as-obtained capacitance is compared with previously reported literature values (figure 9(c)) e.g., $\text{TiO}_2/\text{powder}$ ($33\text{--}181\text{ }\mu\text{F/cm}^2$ at 100 to 1 mV/s),^[27] double-layer capacitance from colloidal RuO_2 ($300\text{ }\mu\text{F/cm}^2$),^[28] three-dimensional porous MnO_2 structure ($70\text{--}90\text{ }\mu\text{F/cm}^2$).^[29]

Based on both experimental and simulation results, the anomalous electrochemical enhancement of Ti_2O_3 under the annealed and IR illumination conditions can be explained by its bandgap and the subsequent bandgap crossover of $\text{Ti } 3d a_{1g}$ and e_g^π levels as explained by Goodenough.[30] Figure 10(a) schematically depicts the three-dimensional network of Ti_2O_3 coated on the electrode plane for the symmetric electrochemical capacitor.[31] The crystal structure of Ti_2O_3 mainly consists of honeycomb lattice in parallel layers formed by Ti^{3+} ions in the a - b plane, which are paired along the c -axis as dimers and each ion is surrounded by the O^{2-} ions.[32] The response of pristine semiconductor Ti_2O_3 toward electrochemical capacitance is limited by the space-charge region as depicted by figure 10(b) near its surface.[1] The band overlapping at higher annealing temperature changes the density and distribution of the resulting delocalized electrons leading to a jellylike structureless distribution (schematic in figure 10(c)).[1] The rise in temperature from RT to 300 °C and an enhanced EDLC response clearly indicated a large charge accumulation on the surface with more DOS, as explained earlier in figure 3.

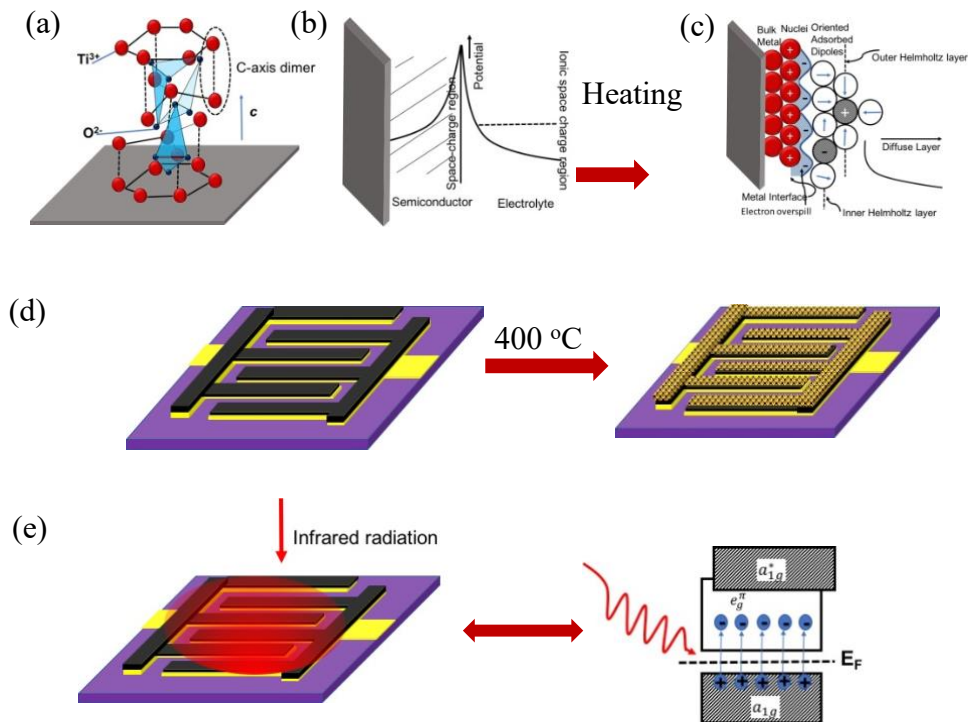


Figure 10. (a) Schematic representation of crystal structure of Ti_2O_3 . (b) Space charge distribution of charge carriers within the pristine semiconducting Ti_2O_3 near the electrode/electrolyte interface. (c) Charge layer formation at the interface of metallic Ti_2O_3 and electrolyte (both the figures (b) and (c) are adapted from reference 1). (d) Schematic diagram to depict the surface transformation of Ti_2O_3 into TiO_2 at 400 °C in the device. (e) IR interaction of the electrochemical capacitor (left) and excitons generation across the bandgap of pristine Ti_2O_3 .

As mentioned in our simulation results that the structural disorder in Ti–Ti dimers along the c –axis allowing Ti ions hopping to the a – b plane via $e \frac{\pi}{g}$ channel possibly attributes to the anomaly in electrochemical capacitance response.[32] Although we have not observed any significant changes in the lattice parameters in the XRD measurements, these localized distortions of the dimers are reported by Hwang *et al.*[33] through the X–ray absorption fine structure measurements. Therefore, sharing the $3d$ electrons between the c –axis and basal–plane orbitals enhances the polarizability following the charge hopping[34] led to an anomalous enhancement in electrochemical capacitance at 300 °C. Further annealing at 400 °C has shown a clear signature of appearance of TiO_2 phase and coexistence of both Ti_2O_3 and TiO_2 as described earlier and schematically depicted in figure 10(d) by following the phase transformation from $\text{Ti}_2\text{O}_3 \rightarrow \text{TiO}_{2-x} \rightarrow \text{TiO}_2$ as given by Li *et al.*[5] The IR interaction with pristine and annealed Ti_2O_3 can be understood through the additionally enhanced space–charge contribution from the transition across the bandgap as shown in figure 10(e). The IR induced enhanced electrochemical capacitance in annealed Ti_2O_3 after transition to a metallic state could be attributed to the thermal excitations through the vibration of crystal lattice.

Conclusion

The insulator to metal transition in Mott–insulator, Ti_2O_3 is exploited for the electrochemical capacitance. An extraordinary large enhancement in electrochemical capacitance of ~560% is

observed after annealing the sample at 300 °C compared to the other annealing conditions at 200 °C and 400 °C. Further pristine Ti₂O₃ provided an enhancement of ~3500% in electrochemical capacitance upon infrared radiation interaction. These extraordinary enhancements in the electrochemical responses are explained based on the interaction of Ti ions with the O ions upon heating conditions and resulting localized hybridization leading to the electron spill over the surface of the metallic Ti₂O₃. The DFT simulations further supported the enhanced participation of surface states with the increase in temperature, which strongly supports our experimental findings.

References

- [1] B.E. Conway, *Electrochemical Supercapacitors-Scientific Fundamentals and Technological Applications*-Springer (1999).
- [2] P. Simon, Y. Gogotsi, Perspectives for electrochemical capacitors and related devices, *Nat. Mater.* 19 (2020) 1151–1163. <https://doi.org/10.1038/s41563-020-0747-z>.
- [3] J. Wang, Y. Li, L. Deng, N. Wei, Y. Weng, S. Dong, D. Qi, J. Qiu, X. Chen, T. Wu, High-Performance Photothermal Conversion of Narrow-Bandgap Ti₂O₃ Nanoparticles, *Adv. Mater.* 29 (2017) 1–6. <https://doi.org/10.1002/adma.201603730>.
- [4] X. Yu, Y. Li, X. Hu, D. Zhang, Y. Tao, Z. Liu, Y. He, M.A. Haque, Z. Liu, T. Wu, Q.J. Wang, Narrow bandgap oxide nanoparticles coupled with graphene for high performance mid-infrared photodetection, *Nat. Commun.* 9 (2018) 1–8. <https://doi.org/10.1038/s41467-018-06776-z>.
- [5] Y. Li, Y. Yang, X. Shu, D. Wan, N. Wei, X. Yu, M.B.H. Breese, T. Venkatesan, J.M. Xue, Y. Liu, S. Li, T. Wu, J. Chen, From Titanium Sesquioxide to Titanium Dioxide: Oxidation-Induced Structural, Phase, and Property Evolution, *Chem. Mater.* 30 (2018)

- 4383–4392. <https://doi.org/10.1021/acs.chemmater.8b01739>.
- [6] C.J. Dahlman, G. Leblanc, A. Bergerud, C. Staller, J. Adair, D.J. Milliron, Electrochemically Induced Transformations of Vanadium Dioxide Nanocrystals, *Nano Lett.* 16 (2016) 6021–6027. <https://doi.org/10.1021/acs.nanolett.6b01756>.
- [7] R. Basu, S. Ghosh, S. Bera, A. Das, S. Dhara, Phase-pure VO₂ nanoporous structure for binder-free supercapacitor performances, *Sci. Rep.* 9 (2019) 1–11. <https://doi.org/10.1038/s41598-019-40225-1>.
- [8] S. Nandi, R. Tripathi, G. Das Adhikary, P. Kumar, A. Misra, Ultrahigh Infrared Photoresponse in Titanium Sesquioxide at Mott-Insulator Transition, *Adv. Mater. Interfaces.* 7 (2020) 1–7. <https://doi.org/10.1002/admi.202001091>.
- [9] M.A. Afifi, M.M. Abdel-Aziz, I.S. Yahia, M. Fadel, L.A. Wahab, Transport properties of polycrystalline TiO₂ and Ti₂O₃ as semiconducting oxides, *J. Alloys Compd.* 455 (2008) 92–97. <https://doi.org/10.1016/j.jallcom.2007.01.156>.
- [10] M. Uno, S. Nishimoto, Y. Kameshima, M. Miyake, Hydrogen production by mechanochemical reaction of Ti₂O₃ in water, *Int. J. Hydrogen Energy.* 38 (2013) 15049–15054. <https://doi.org/10.1016/j.ijhydene.2013.09.118>.
- [11] S.F. Shaikh, R.S. Mane, B.K. Min, Y.J. Hwang, O.S. Joo, D-sorbitol-induced phase control of TiO₂ nanoparticles and its application for dye-sensitized solar cells, *Sci. Rep.* 6 (2016) 1–10. <https://doi.org/10.1038/srep20103>.
- [12] M. Xu, A. Zada, R. Yan, H. Li, N. Sun, Y. Qu, Ti₂O₃/TiO₂ heterophase junctions with enhanced charge separation and spatially separated active sites for photocatalytic CO₂ reduction, *Phys. Chem. Chem. Phys.* 22 (2020) 4526–4532. <https://doi.org/10.1039/c9cp05147c>.
- [13] V. Singh, J.J. Pulikkotil, Electronic phase transition and transport properties of Ti₂O₃, *J. Alloys Compd.* 658 (2016) 430–434. <https://doi.org/10.1016/j.jallcom.2015.10.203>.

- [14] V. Mishra, A. Sagdeo, V. Kumar, M.K. Warshi, H.M. Rai, S.K. Saxena, D.R. Roy, V. Mishra, R. Kumar, P.R. Sagdeo, Electronic and optical properties of BaTiO₃ across tetragonal to cubic phase transition: An experimental and theoretical investigation, *J. Appl. Phys.* 122 (2017). <https://doi.org/10.1063/1.4997939>.
- [15] V. Mishra, M.K. Warshi, A. Sati, A. Kumar, V. Mishra, A. Sagdeo, R. Kumar, P.R. Sagdeo, Diffuse reflectance spectroscopy: An effective tool to probe the defect states in wide band gap semiconducting materials, *Mater. Sci. Semicond. Process.* 86 (2018) 151–156. <https://doi.org/10.1016/j.mssp.2018.06.025>.
- [16] V. Mishra, M.K. Warshi, A. Sati, A. Kumar, V. Mishra, R. Kumar, P.R. Sagdeo, Investigation of temperature-dependent optical properties of TiO₂ using diffuse reflectance spectroscopy, *SN Appl. Sci.* 1 (2019) 1–8. <https://doi.org/10.1007/s42452-019-0253-6>.
- [17] S. Kumar, S. Telpande, V. Manikandan, P. Kumar, A. Misra, Novel electrode geometry for high performance CF/Fe₂O₃ based planar solid state micro-electrochemical capacitors, *Nanoscale.* 12 (2020) 19438–19449. <https://doi.org/10.1039/d0nr04410e>.
- [18] J. Wang, J. Polleux, J. Lim, B. Dunn, Pseudocapacitive contributions to electrochemical energy storage in TiO₂ (anatase) nanoparticles, *J. Phys. Chem. C.* 111 (2007) 14925–14931. <https://doi.org/10.1021/jp074464w>.
- [19] T. Brezesinski, J. Wang, S.H. Tolbert, B. Dunn, Ordered mesoporous α -MoO₃ with iso-oriented nanocrystalline walls for thin-film pseudocapacitors, *Nat. Mater.* 9 (2010) 146–151. <https://doi.org/10.1038/nmat2612>.
- [20] Y. Gogotsi, P. Simon, True Performance Metrics in Electrochemical Energy Storage, *Science* (80-.). 334 (2011) 917–918.
- [21] S.M. Lee, Y.J. Park, D. Van Lam, J.H. Kim, K. Lee, Effects of annealing on electrochemical performance in graphene/V₂O₅ supercapacitor, *Appl. Surf. Sci.* 512

- (2020) 145626. <https://doi.org/10.1016/j.apsusc.2020.145626>.
- [22] T.R. Jow, J.P. Zheng, Amorphous thin film ruthenium oxide as an electrode material for electrochemical capacitors, *Mater. Res. Soc. Symp. - Proc.* 393 (1995) 433–438. <https://doi.org/10.1557/proc-393-433>.
- [23] M. Beidaghi, C. Wang, Micro-supercapacitors based on interdigital electrodes of reduced graphene oxide and carbon nanotube composites with ultrahigh power handling performance, *Adv. Funct. Mater.* 22 (2012) 4501–4510. <https://doi.org/10.1002/adfm.201201292>.
- [24] D. Pech, M. Brunet, H. Durou, P. Huang, V. Mochalin, Y. Gogotsi, P.L. Taberna, P. Simon, Ultrahigh-power micrometre-sized supercapacitors based on onion-like carbon, *Nat. Nanotechnol.* 5 (2010) 651–654. <https://doi.org/10.1038/nnano.2010.162>.
- [25] P.L. Taberna, P. Simon, J.F. Fauvarque, Electrochemical Characteristics and Impedance Spectroscopy Studies of Carbon-Carbon Supercapacitors, *J. Electrochem. Soc.* 150 (2003) A292. <https://doi.org/10.1149/1.1543948>.
- [26] M.F. El-Kady, R.B. Kaner, Scalable fabrication of high-power graphene micro-supercapacitors for flexible and on-chip energy storage, *Nat. Commun.* 4 (2013). <https://doi.org/10.1038/ncomms2446>.
- [27] M. Salari, S.H. Aboutalebi, K. Konstantinov, H.K. Liu, A highly ordered titania nanotube array as a supercapacitor electrode, *Phys. Chem. Chem. Phys.* 13 (2011) 5038–5041. <https://doi.org/10.1039/c0cp02054k>.
- [28] J.M. Kleijn, J. Lyklema, The electrical double layer on oxides: Specific adsorption of chloride and methylviologen on ruthenium dioxide, *J. Colloid Interface Sci.* 120 (1987) 511–522. [https://doi.org/10.1016/0021-9797\(87\)90378-X](https://doi.org/10.1016/0021-9797(87)90378-X).
- [29] Y. Wang, Y. Song, Y. Xia, Electrochemical capacitors: Mechanism, materials, systems, characterization and applications, *Chem. Soc. Rev.* 45 (2016) 5925–5950.

<https://doi.org/10.1039/c5cs00580a>.

- [30] L.L. Van Zandt, J.M. Honig, J.B. Goodenough, Resistivity and magnetic order in Ti_2O_3 , *J. Appl. Phys.* 39 (1968) 594–595. <https://doi.org/10.1063/1.2163536>.
- [31] M. Uchida, J. Fujioka, Y. Onose, Y. Tokura, Charge dynamics in thermally and doping induced insulator-metal transitions of $(\text{Ti}_{1-x}\text{V}_x)_2\text{O}_3$, *Phys. Rev. Lett.* 101 (2008) 8–11. <https://doi.org/10.1103/PhysRevLett.101.066406>.
- [32] H. Sato, A. Tanaka, M. Sawada, F. Iga, K. Tsuji, M. Tsubota, M. Takemura, K. Yaji, M. Nagira, A. Kimura, T. Takabatake, H. Namatame, M. Taniguchi, Ti 3d orbital change across metal-insulator transition in Ti_2O_3 : Polarization-dependent soft X-ray absorption spectroscopy at Ti 2p edge, *J. Phys. Soc. Japan.* 75 (2006) 75–78. <https://doi.org/10.1143/JPSJ.75.053702>.
- [33] I.H. Hwang, B. Jiang, Z. Jin, C.I. Park, S.W. Han, Anomalous structural disorder and distortion in metal-to-insulator-transition Ti_2O_3 , *J. Appl. Phys.* 119 (2016). <https://doi.org/10.1063/1.4939290>.
- [34] A. Mooradian, P. Raccach, Raman Study of the Semiconductor-Metal Transition in Ti_2O_3 , *Phys. Rev. B.* 3 (1970) 4253–4256.